Raman Imaging

Shona Stewart, Ryan J. Priore, Matthew P. Nelson, and Patrick J. Treado

ChemImage Corporation, Pittsburgh, Pennsylvania 15208; email: treado@chemimage.com

Annu. Rev. Anal. Chem. 2012. 5:337–60

First published online as a Review in Advance on April 9, 2012

The *Annual Review of Analytical Chemistry* is online at anchem.annualreviews.org

This article's doi: 10.1146/annurev-anchem-062011-143152

1936-1327/12/0719-0337$20.00

Keywords

Raman molecular imaging, wide-field Raman imaging, Raman chemical imaging, CARS, SERS imaging, standoff Raman imaging

Abstract

The past decade has seen an enormous increase in the number and breadth of imaging techniques developed for analysis in many industries, including pharmaceuticals, food, and especially biomedicine. Rather than accept single-dimensional forms of information, users now demand multidimensional assessment of samples. High specificity and the need for little or no sample preparation make Raman imaging a highly attractive analytical technique and provide motivation for continuing advances in its supporting technology and utilization. This review discusses the current tools employed in Raman imaging, the recent advances, and the major applications in this ever-growing analytical field.

1. INTRODUCTION

Raman imaging techniques have emerged, greatly improved, and transformed in recent years because of a growing desire for multidimensional analytical information. Advances in laser technology, filters, spectrometers, detection devices, processing algorithms, and computer technology have contributed to the renaissance of Raman imaging as a methodology. Use of Raman scattering as an analytical tool is of significant interest because of its high specificity, low sensitivity to water, and requirement for minimal sample preparation.

The spontaneous Raman effect is a scattering phenomenon defined by a two-photon event. An incident photon induces a change in polarizability, a deformation of the electron cloud of a molecule with respect to its vibrational motion. The electron cloud deformation results in an induced dipole moment, a partial positive/negative charge across a molecular bond existing in a virtual state. A photon is immediately emitted from the molecular bond in order for it to return to a ground state. Most photons are emitted at the same frequency as the incident photon. This phenomenon is known as Rayleigh scattering. Raman scattering occurs when the photons are emitted at a frequency different from that of the incident photons. Stokes Raman scattering occurs when a scattered photon decreases in frequency (energy) compared with that of the incident photon. Anti-Stokes Raman scattering occurs when a scattered photon increases in frequency (energy) compared with that of the incident photon.

Raman chemical imaging combines Raman spectroscopy with digital imaging technology to visualize material chemical composition and molecular structure at the same time. Collecting data in an imaging mode reduces the effect of interferents in the field of view because each pixel in an image contains chemical data specific to the species in that pixel, which corresponds to a finite sampling volume.

2. MODES OF IMAGING

Raman imaging may produce hundreds, thousands, or even millions of independent, spatially resolved Raman spectra, typically without the need for sample preparation. **Figure 1** illustrates a Raman hyperspectral data cube consisting of *x* and *y* spatial dimensions, as well as a wavelength dimension. In this data cube collected from a heterogeneous nasal spray suspension (**Figure 1*a***), each pixel corresponds to a Raman spectrum associated with the material imaged at that spatial location (**Figure 1*b***). **Figure 1*c*** compares two Raman spectra with the mean spectrum extracted from the hyperspectral data cube. The mean spectrum represents a bulk spectral measurement and has the potential to envelop signals from all interferents, including a fluorescence background, in the field of view. The analytical value of Raman imaging is realized when discrete spectroscopic information can be obtained from a unique spatial location within a sample.

Advances in laser technology, Rayleigh line rejection filters, imaging spectrometers, imaging detectors, and data-processing computers have improved instruments' ease of use and have increased the robustness of the hardware. Developments in measurement automation have extended Raman imaging to users other than scientists. Raman imaging techniques may be broadly classified as either spontaneous or nonlinear.

2.1. Spontaneous Raman Imaging Modes

Spontaneous Raman imaging refers to Raman imaging based on traditional, single photon–induced Raman spectroscopy. Since the development of the first Raman microprobe in the 1970s, most Raman imaging has been performed with scanning-based instrumentation coupled to optical

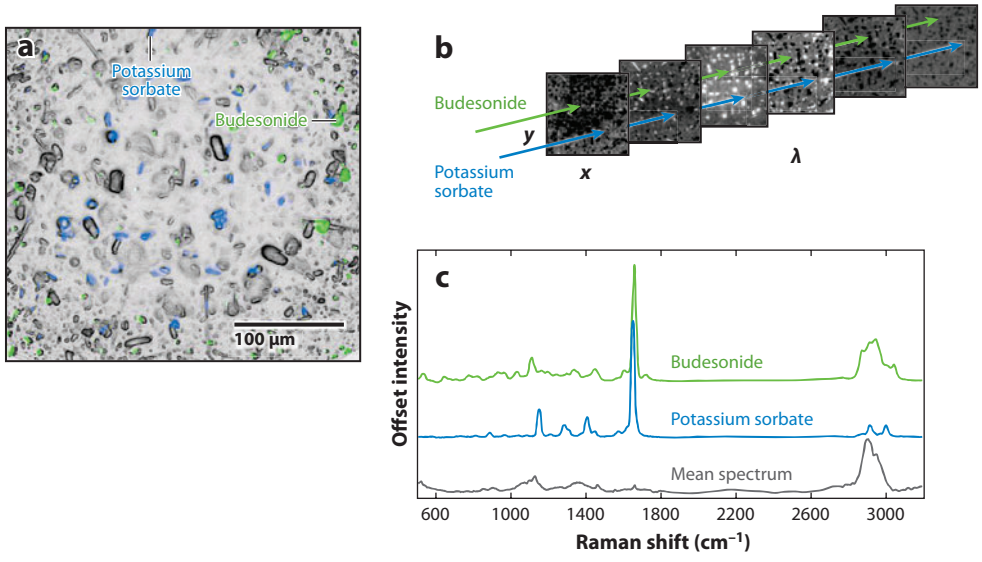

Figure 1

Example of Raman imaging applied to a nasal spray suspension droplet. (*a*) False-colored Raman chemical image overlaid on an optical micrograph in bright-field reflection mode. (*b*) Raman chemical image composed of both spatial and spectral dimensions. (*c*) Raman spectra from two ingredients, budesonide (*green*) and potassium sorbate (*blue*), as well as the mean sample spectrum (*gray*) extracted from the Raman chemical image. Reproduced from Reference 77 with permission.

microscopes (1). Scanning instrumentation produces Raman "maps" of a sample's surface. A source laser is focused onto the sample and scanned across multiple spatial locations while one or more spectra are collected (2). Scanning methods can be further divided into point mapping and line scanning. Wide-field instrumentation illuminates the entire sample field of view with a source laser and typically analyzes discrete frequencies of light as a function of time. **Figure 2** provides a summary of scanning and wide-field Raman imaging techniques.

2.1.1. Point mapping. Point-mapping Raman instrumentation employs high-precision sample stages to control the lateral and axial coordinates of a sample while raster scanning a tightly focused laser spot across a sample surface. A Raman spectrum is acquired at each spatial location with either a dispersive spectrometer or interferometer to generate a hyperspectral data cube. Spectral resolutions from 1 to 4 cm^{-1} (3) may be achieved; spatial resolution can range from 2 to 5 µm for visible-region Raman microscopes and from 6 to 25 µm for Fourier transform near-IR (NIR) Raman microscopes.

Current microscopic point-mapping Raman instrumentation operates in a confocal configuration, which reduces the chance of background fluorescence and effects of secondary scattering but increases the chance of localized photo-induced damage. In the past, scan times of hours to days were not uncommon for point-by-point experiments, which limited their utility for routine material characterization. Poorly defined axial sampling further complicated confocal point mapping (4, 5). Recent advances in instrumentation components have enabled the acquisition of spectra on the order of milliseconds and hyperspectral data cubes on the order of minutes for strong Raman scatterers.

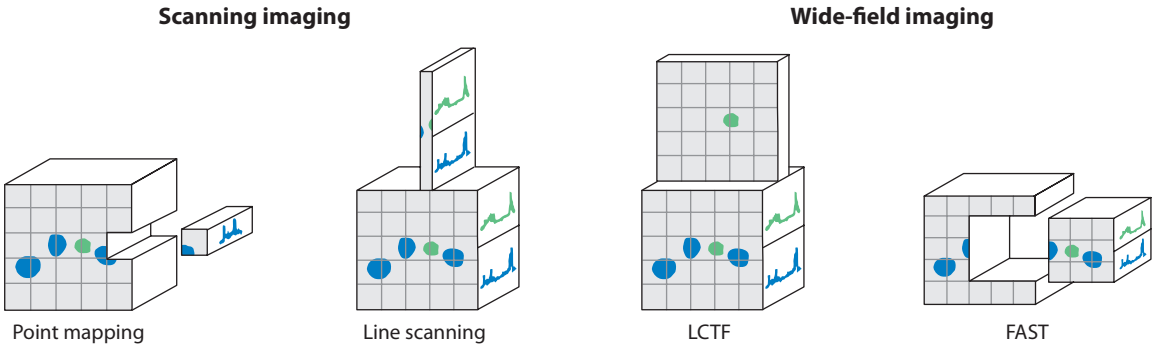

Method	Advantages	Limitations
Point mapping	• High spectral resolution • Full spectral coverage • Confocal	• Low-definition images • Slow (limited by scan rates, autofocus, photobleaching) • Laser-induced sample damage
Line scanning	• Moderately efficient imaging • Full spectral range • Confocal • High spectral resolution	• Field-curvature artifacts • Moderately slow (limited by autofocus, photobleaching) • Moderate-definition images
LCTF	• Highly efficient image collection • Diffraction-limited spatial resolution • High-definition images • High spectral resolution • Wide-field photobleaching	• High throughput • Inefficient spectral collection
FAST	• Moderately efficient imaging • Full spectral range • High spectral resolution	• Moderate-definition images

Figure 2

Comparison between scanning and wide-field Raman imaging techniques. Abbreviations: FAST, fiber array spectral translation; LCTF, liquid crystal tunable filter.

2.1.2. Line scanning. Line scanning (6–8) is an extension of point mapping wherein a source laser beam is shaped into a line through the use of cylindrical optics or a scanning mechanism such as a moving mirror. An automated sample stage moves the sample perpendicular to the incident laser line. The collected Raman signal is oriented parallel to the entrance slit of a dispersive spectrometer and consequently onto a two-dimensional array detector. A spectrum is then captured for each row of the detector [e.g., a charge-coupled device (CCD)] corresponding to a spatial location along the length of the laser line. The image spatial resolution in the direction parallel to the laser line is determined by the magnification of the collection optic and the pixel size associated with the detector, yielding diffraction-limited spatial resolution. In the direction perpendicular to the laser line, spatial resolution is dictated by the laser beam width and the precision of the sample-stage translation. Microscopic, line-scanning Raman imaging systems are commercially available; however, these systems are not as widely used as point-mapping systems.

2.1.3. Wide-field Raman imaging. The entire sample field of view is illuminated with laser light and analyzed in parallel for wide-field (i.e., global) imaging. Most of these techniques analyze discrete frequencies of light as a function of time by employing a wide-aperture optical

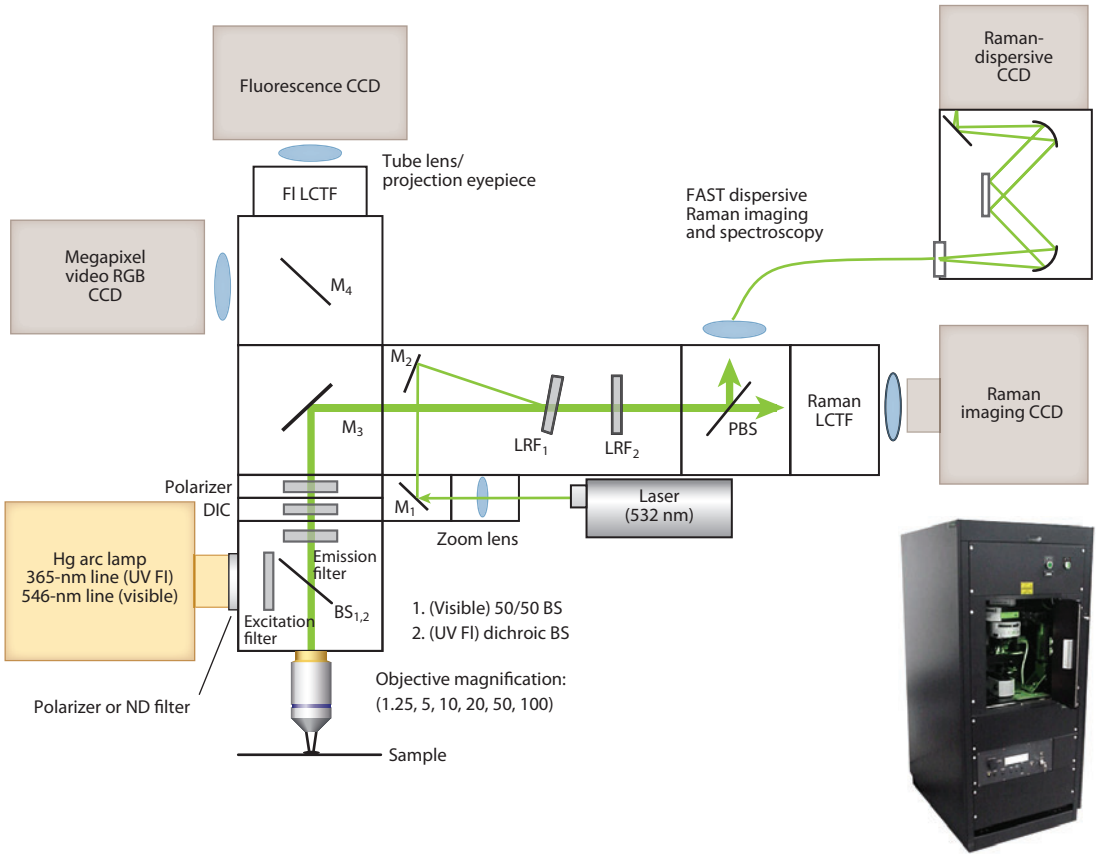

Figure 3

Schematic of a ChemImage Falcon II™ wide-field Raman chemical imaging microscope. Abbreviations: BS, beam splitter; CCD, charge-coupled device; DIC, differential contrast; FI, fluorescence imaging; LCTF, liquid crystal tunable filter; LRF, laser rejection filter; ND, neutral density; PBS, polarized beam splitter. Reproduced from Reference 104 with permission.

filter. **Figure 3** illustrates a schematic of a Falcon II™ Raman chemical imaging microscope (ChemImage Corporation, Pittsburgh, Pennsylvania) for wide-field Raman imaging.

The duration of a wide-field experiment, T_w, is proportional to the number of spectral channels, m, instead of the number of image pixels, n, as in point-mapping and line-scanning approaches, because two spatial dimensions are collected simultaneously. The measurement-time benefits of wide-field imaging are realized when m is less than n for point-by-point mapping or less than $\sqrt{n}$ for line scanning. Assuming that there is a comparable laser power density to the point-mapping and line-scanning approaches as well as a square image, the experimentation-time relationships between wide-field and point-mapping and line-scanning approaches are as shown in Equations 1 and 2:

$$T_w = \left(\frac{m}{n}\right) T_p; \quad (1)$$

$$T_w = \left(\frac{m}{\sqrt{n}}\right) T_l. \quad (2)$$

For many material characterization applications, only a very small number of spectral bands are required for analyte discrimination, which allows rapid wavelength tuning to support dynamic or real-time Raman imaging. Dynamic Raman imaging is not feasible with scanning methods because a reduction in the number of spectral channels has no real impact on experiment times, given that the entire spectrum is captured simultaneously by a spectrometer. Time reduction with scanning methods negatively affects the spatial resolution or field of view of the resultant Raman image.

As opposed to the size of a focused laser spot, spatial resolution (r) for wide-field imaging is dictated by a convolution of diffraction theory, CCD pixel size, and magnification. The Sparrow criterion defines the spatial resolution of an optical system as the distance between two point objects at which contrast is immeasurable, and the more common diffraction-limited Rayleigh criterion defines the spatial resolution as $r = \frac{1.22\lambda}{2NA}$, where λ is the wavelength of light and NA is the numerical aperture of the light-gathering optic. The Rayleigh criterion does not limit the ability to image even smaller features of brightly scattering materials, and as such, it is perceived as a spatial resolution guide and not as an absolute limit (9).

Various wide-field Raman imaging instrumental developments have occurred over the past two decades; these developments include tunable lasers and fixed (10) or rotating (6) dielectric filters, acousto-optic tunable filters (9, 11–13), liquid crystal tunable filters (LCTFs) (9, 14), and fiber array assemblies (15–19). Current wide-field Raman imaging methodologies are described in detail in previously published reviews (e.g., Reference 20). In this review, we focus on the two most commonly utilized methods: LCTFs and fiber array technologies.

2.1.3.1. Liquid crystal imaging spectrometers. Most liquid crystal imaging spectrometers can provide diffraction-limited spatial resolution with spectral resolutions rivaling that of a single-stage dispersive monochromator. LCTFs are computer-controlled, electro-optically tunable devices with no moving parts; they can produce a user-defined single band pass of light. LCTFs also provide high out-of-passband rejection efficiencies, broad free spectral ranges, operation in the visible and NIR portions of the spectrum (400–2,500 nm), and high overall étendues. Limitations of liquid crystal imaging spectrometers include inefficient full spectral data collection and low to moderate throughput (in some designs) (14, 21, 22).

To address increasing demands for improved optical throughput and thermal stability, investigators have developed a new class of liquid crystal imaging spectrometer: the multiconjugate filter (MCF) (23). The MCF combines the high transmittance associated with a Solc filter (24) and the high out-of-band rejection efficiency of the Lyot filter (25). The MCF differs from previous-generation devices in that each stage of the filter has an increased finesse—1.5 times the finesse of Evans filters and 2 times the finesse of a typical Lyot design. The MCF also utilizes a passive temperature-correction strategy to achieve a thermal stability that is superior to that of Evans filters.

2.1.3.2. Fiber array Raman imaging. A more recent approach to Raman imaging that has gained popularity in the last decade is based on fiber optic arrays. Names for this technology include fiber array spectral translation (FAST) (26), dimension-reduction arrays (16–18), and fiber image compression (19). Two spatial dimensions and one spectral dimension of data may be collected simultaneously with fiber arrays by focusing Raman light captured from a globally illuminated field of view onto the proximal end of a two-dimensional array of optical fibers. The distal end of the fiber array is then drawn into a linear array and inserted parallel into the entrance slit of a dispersive spectrometer equipped with an imaging-format CCD detector. In a single-frame acquisition, all of the spatial and spectral information is obtained simultaneously. Software is then used to unravel the embedded spatial and spectral information by reconstructing the data into a hyperspectral data cube (**Figure 4**).

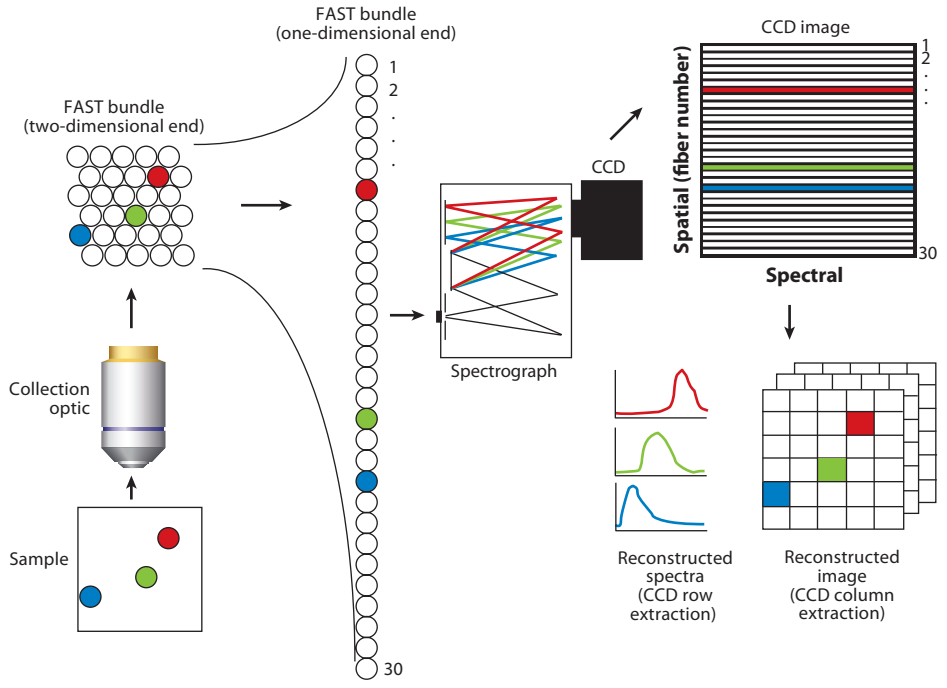

Figure 4

Fiber array spectral translation (FAST) configuration for wide-field Raman imaging. The spatial dimensions of the chemical image are reconstructed from discrete rows of an optical spectrometer and a fiber optic pair. Abbreviation: CCD, charge-coupled device.

Fiber arrays have an inherent speed advantage over competing Raman imaging techniques for applications that require substantial spectral information but only limited spatial information. For reasonably bright Raman scatterers, the data-acquisition time for a single field of view is comparable to the time it takes to acquire a single dispersive spectrum. Equations 3, 4, and 5 show the relationship between the experiment time required for a fiber array Raman imaging system and those required for point-mapping, line-scanning, and (wavelength scanning) wide-field Raman imaging instruments, respectively. In these equations, ROI is the number of regions of interest acquired in the experiment. The assumptions that apply to Equations 1 and 2 also apply to Equations 3, 4, and 5, in addition to comparable laser power density at each spatial location:

$$T_{\mathrm{FAST}} = \frac{T_p}{n} \cdot \mathrm{ROI}; \tag{3}$$

$$T_{\mathrm{FAST}} = \frac{T_l}{\sqrt{n}} \cdot \mathrm{ROI}; \tag{4}$$

$$T_{\mathrm{FAST}} = \frac{T_w}{m} \cdot \mathrm{ROI}. \tag{5}$$

Another advantage of using fiber arrays for Raman imaging is that spectral resolution and spectral coverage are governed by the dispersion properties of the dispersive spectrometer. Fiber array image fidelity (the number of pixels) is limited by the number of CCD detector rows. High-definition images may be obtained with this technique through the collection and reconstruction

of fiber array Raman images from multiple adjacent fields of view. Alternatively, multiple spectrometers, each equipped with CCDs, may be used to increase image definition. A drawback to the use of fiber arrays for Raman imaging is their susceptibility to pixel-to-pixel cross talk as a result of imperfect image performance of modern spectrometers. Cross talk may be minimized by intentional spacing of fibers or specialized fiber mapping arrangements in which adjacent fibers in the object field are also juxtaposed in the image field.

2.2. Nonlinear Raman Imaging Modes

The low sensitivity of conventional Raman techniques has led to recent advances in nonlinear Raman microscopic methodologies. Coherent Raman scattering techniques, which include coherent anti-Stokes Raman scattering (CARS) and stimulated Raman scattering (SRS) microscopy, have become more prolific in recent years; therefore, the methodologies, instrumentation, and technology involved continue to change.

2.2.1. Coherent anti-Stokes Raman scattering imaging. The phenomenon of CARS was first reported in 1965 by Maker & Terhune (27), but only in 1999, when a new CARS method was introduced by Zumbusch et al. (28), did the technology begin to generate real interest. The principles of CARS have been reviewed by numerous groups (29). CARS is a four-wave mixing process that uses two synchronized pulsed lasers, at different wavelengths, for sample excitation. During this process, one laser generates a pump field, E_p (ω_p), and the other generates a Stokes field, E_s (ω_s). Both fields interact with a sample to generate an anti-Stokes field, E_{as}, at a frequency of $2\omega_p$–ω_s (29). If ω_p–ω_s is tuned to a Raman band, the CARS signal is significantly enhanced (30). The inherent signal enhancement resulting from the CARS technique renders it suitable for the imaging regime. Spectra with a high signal-to-noise ratio result in faster acquisition rates. Inherent to the technique are submicrometer spatial resolution and three-dimensional sectioning (31–34). A significant limitation of CARS is the nonresonant background generated by the nonlinear electronic response of the sample mediated through virtual states (35). The CARS imaging microscope is composed of a fast scanning microscope and an ultrafast light source, such as a picosecond laser. Scanning of the focal spot is accomplished either by scanning the sample stage or by angle scanning the incident pump and Stokes beams (36).

2.2.2. Stimulated Raman scattering imaging. Since its discovery in the 1970s, SRS has been the subject of interest in numerous systems (37–39). Like CARS, SRS arises from the nonlinear interaction between molecules and a laser pulse. A pump photon is converted into a Stokes photon when a molecule is excited from the vibrational ground state into the first vibrational excited state. In effect, SRS probes the excited vibrational population rather than the vibrational coherence observed by CARS (40, 41). SRS does not suffer from the nonresonant background experienced by CARS microscopy. Min et al. (35) show that as a result, SRS spectra can be compared with those of spontaneous Raman spectra, thereby facilitating assignments based on Raman literature. The ability to perform such assignments makes SRS a more favorable technique for Raman imaging than CARS (42).

2.3. Emerging Modes of Imaging

New methods of imaging are continually being introduced. Those demonstrating the most promise for acceptance in the field are discussed in this section. Many of these emerging techniques, such as surface-enhanced Raman scattering (SERS) imaging, standoff Raman imaging, and spatially

offset Raman scattering (SORS) imaging, are extensions of existing spectroscopic procedures into the imaging regime. Others, such as compressive sensing, have been introduced specifically to exploit the art of imaging to its fullest extent.

2.3.1. Surface-enhanced Raman scattering imaging. The strategy of enhancing a Raman signal by causing a sample to interact with SERS-active particles or substrate was developed three decades ago and continues to evolve. The two primary principles behind SERS are still a matter of debate: The electromagnetic theory considers the excitation of localized surface plasmons, and the chemical theory considers the formation of charge-transfer complexes between sample and substrate.

Raman imaging of SERS substrates has appeared in the literature only infrequently (43, 44) because of the heterogeneous nature of the enhancement, even from highly uniform substrates. Most currently favored SERS imaging substrates are based on nanoparticles, which can be inserted into materials or taken up by or tethered to live cells (45–48). This methodology has been used to observe fungal cell growth (49), mammalian cells (50), bacterial cells (51), cancer markers (52, 53), and small live animals (48, 54). However, even highly nanopatterned substrates often do not provide homogeneous surfaces for SERS measurements. Gough & Kaminskyj (49) observed what they termed hot spots when measuring the growth of fungal hyphae across their nanopatterned substrate. They could not determine quantitative enhancement due to the heterogeneity of the image spectra. More promising results were obtained in a recent study of cancer markers on a gold substrate (52).

2.3.2. Standoff Raman imaging. The use of telescopes with Raman spectroscopic systems has enabled the development of standoff measurements. Standoff Raman measurements of various specimens have been reported up to 500 m. This methodology was initially applied to samples that could not be reached or safely approached. Detection of minerals on planetary surfaces (55), explosive residues (56), and atmospheric gases (57) were initially studied through the standoff approach.

To detect weak Raman signals in the presence of interfering backgrounds from large distances, standoff Raman systems typically utilize pulsed lasers with gated, intensified CCD detectors. Tunable filters or FAST bundles are used to achieve standoff Raman imaging (26). High-level image-processing methodologies are also often required in order to reduce background interferences in the images. **Figure 5** illustrates Raman imaging of a Styrofoam™/high-density polyethylene target acquired with a standoff Raman chemical imaging sensor developed by ChemImage Corporation. Data were acquired at a 30-m standoff distance by raster scanning wide-field regions of interest. Through the use of FAST technology, a total of 3,672 spectra were collected in 20 min over 225 cm^2.

More recently, the CARS technique was utilized to collect chemical images of polystyrene, polymethylmethacrylate, dinitrotoluene (DNT), and toluene at a standoff distance of 1 m (58). The polymers and solvent represent a complex chemical environment in which a trace amount of DNT was detected. The target was raster scanned and the spectrally resolved signal processed to form several chemical maps simultaneously. The magnitude of the CARS signal at a particular resonance was monitored relative to the adjacent background to create an intensity map. Bremer et al. (58) demonstrated fast detection of trace quantities of DNT within a complex chemical environment with high chemical specificity.

2.3.3. Spatially offset Raman scattering imaging. First reported in 2005 by Matousek et al. (59, 60), SORS was introduced as a means for retrieving Raman spectra of subsurface layers in

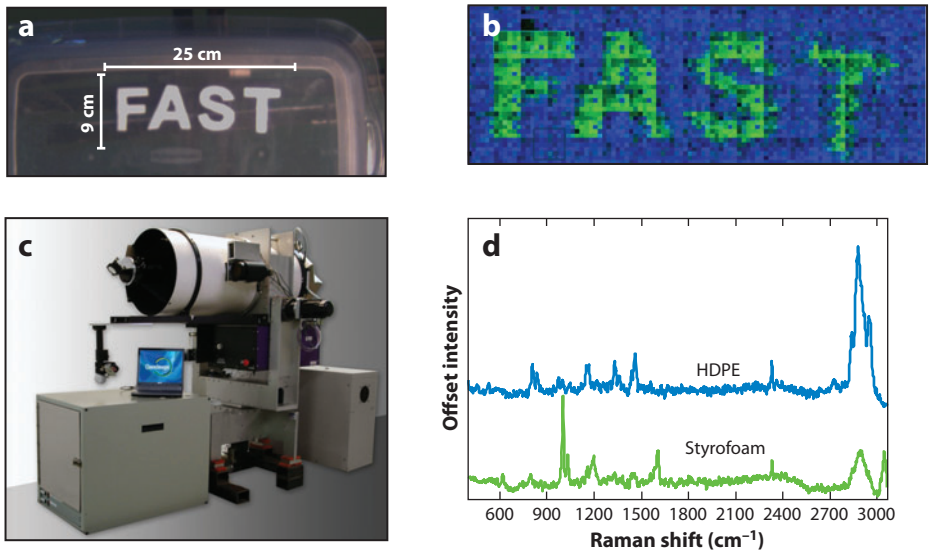

Figure 5

Raman imaging telescope prototype (Raman-ST, ChemImage Corporation, Pittsburgh, Pennsylvania). (*a*) Digital image. (*b*) False-colored Raman image of Styrofoam^{TM} (green; 1,002 cm^{-1}) and high-density polyethylene (HDPE) (blue; 2,882 cm^{-1}). (*c*) Photograph of a Raman-ST sensor. (*d*) Fiber array spectral translation (FAST) Raman spectra associated with each material. Reproduced from Reference 77 with permission.

diffusely scattering media. In a typical Raman instrument, the collection optics are directly above the excited spot. An improvement in the signal-to-noise ratio can be achieved by offsetting the collection optics from the point of incidence of the probe laser beam to acquire the laterally shifted Raman photons. As the collection point is moved away from the incident beam, the contribution of the spectrum from the top layer diminishes much faster than that from deeper layers because Raman photons that are generated deeper within the sample are more likely to migrate laterally before they are emitted from the sample surface.

Because Raman and fluorescence components from the same layer have identical spatial distributions, SORS effectively discriminates against surface layer–generated fluorescence emission (61). In other studies, the SORS signal was enhanced through the use of fiber optic bundles for Raman collection (62, 63). Eliasson et al. (64) demonstrated a simpler variation of SORS by defocusing the collection optics of a Raman system. In another configuration, the incident laser beam is imparted in a transmission mode through the sample; collection of the Raman signal occurred on the other side. This mode of SORS was coupled with SERS in pioneering work by Stone et al. (65, 66), who imaged SERS-active nanoparticles from porcine tissue to a depth of 20 mm. A further variation couples transmission Raman measurements with microcomputed tomography and diffuse optical tomography to produce Raman tomographic images, which provide spatial and compositional information obtained from subsurface molecules (67). **Figure 6** illustrates the reconstruction of Raman tomographic images of bone tissue.

2.3.4. Compressive sensing. Compressive sensing is the process in which a fully resolved waveform or image is reconstructed from a small set of sparse measurements. A sparse sample implies a waveform or image data set with coefficients close to or equal to zero. Compressive sensing

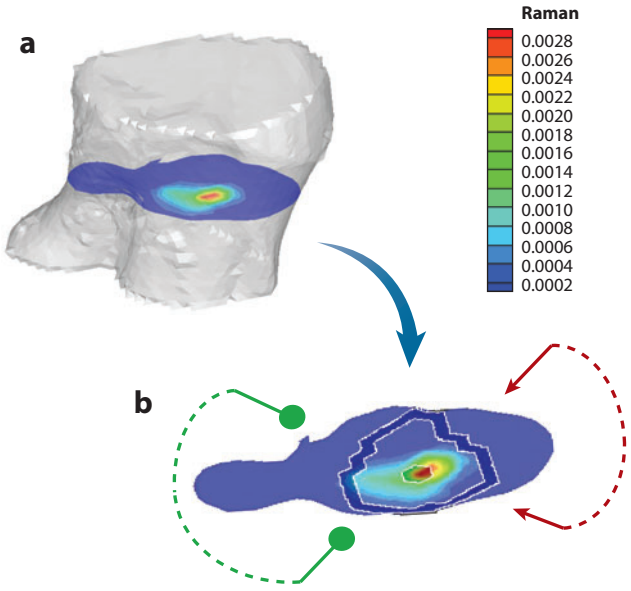

Figure 6

Raman tomographic images of canine bone tissue. (*a*) Three-dimensional mesh of a limb section (*gray*), illustrating the location of a cross section (*blue*) containing the highest Raman scatter intensity. (*b*) Raman intensity at the cross section in panel *a* in pseudocolor overlaid on the microcomputed tomography image of the bone, showing the range of illumination (*red arrows*) and collection (*green dots*) positions. Reproduced from Reference 67 with permission.

utilizes the redundancy in information across the sampled signal, similar to lossy compression algorithms utilized for digital data storage. A fully expanded data set may be created through the solution of an undetermined linear system, an equation wherein the compressive measurements collected are smaller than the size of the original waveform or image. Compressive measurements can ultimately lead to expedited Raman imaging data collections while still preserving most of the original spectroscopic and spatial information.

Over the past decade, compressive sampling techniques have been introduced primarily in the digital imaging community (68, 69); there have also been a few spectroscopic implementations (70–75). Nelson et al. (70) introduced multivariate optical computing, in which a specially designed optical filter physically mimics a regression vector for an analyte- and application-specific data set, thereby allowing a direct measurement of an analyte without the need for subsequent computer processing. This initial study focused on Raman spectroscopic data but has been expanded to other vibrational spectroscopic modes as well as spectroscopic imaging based on optical interference filters (71, 72). Raman spectrometers have also been introduced with a spatial light modulator (i.e., a digital micromirror array or a liquid crystal mask) for the application of a multiwavelength spectroscopic pattern (73, 74).

Davis et al. (75) recently described a point-mapping implementation of multivariate hyperspectral Raman imaging based on compressive detection. This implementation also utilized a spatial light modulator to produce programmable optical filters for the rapid detection of analytes within a modified aspirin core. Compressive detection was achieved through the use of multivariate patterns based on partial least squares or pure component spectral patterns generated by the spatial light modulator. **Figure 7** illustrates a schematic of the point-mapping instrument as well as an example Raman chemical image of an aspirin tablet with theophylline-packed craters. Chemical

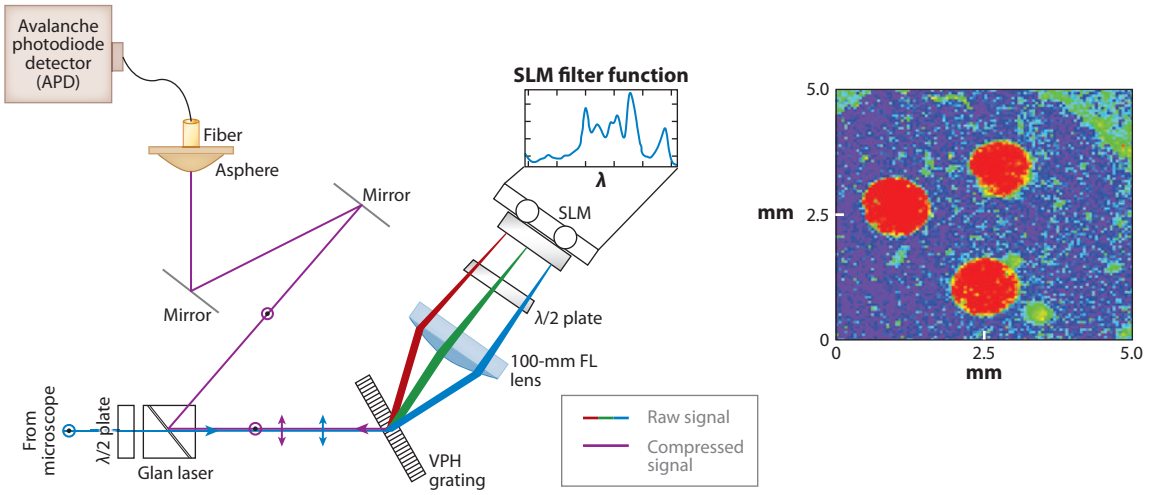

Figure 7

Schematic diagram of a multivariate hyperspectral Raman imaging instrument based on compressive detection. Chemical image (100 × 100 pixels) of an aspirin (*blue*) tablet with theophylline-packed craters (*red*). Abbreviations: FL, focal length; SLM, spatial light modulator; VPH, volume-phase holographic. Reproduced from Reference 75 with permission.

images were collected in less than 1 min over a 5 × 5 mm area on the basis of a >1-ms-per-image pixel data collection.

3. APPLICATIONS

3.1. Pharmaceuticals

Microscopic Raman imaging is an important analytical technique for measuring active pharmaceutical ingredient (API) heterogeneity in tablet cores, controlled release systems, and orally inhaled and nasal drug products (OINDPs) (3, 76). Content uniformity is a measure of the distribution of individual ingredients within a pharmaceutical tablet core, transdermal system, suspension, inhalation product, solid, or suppository. Raman imaging is routinely used to assess product performance degradation. For example, differing levels of solubility in tablet cores can be correlated with the spatial distribution of the API with specific excipients, in addition to the API particle-size distribution (3). **Figure 8** illustrates a confocal Raman imaging analysis of an over-the-counter analgesic tablet. Spatial distributions of the three ingredients (aspirin, acetaminophen, and caffeine) were generated through the use of a direct classical least squares model applied to the spectroscopic data (77).

Raman imaging performs better than NIR imaging for the analysis of common pharmaceutical tablets and granules (78, 79); detection levels as low as 0.2% by weight have been reported (80). The SERS approach is 104 times faster than confocal Raman mapping and has a chemical selectivity superior to that of CARS imaging (81).

A timed-release mechanism ensures the stability of the drug-release level and lesser dosage frequency than that of instant-release formulations. Typical systems either encapsulate the drug

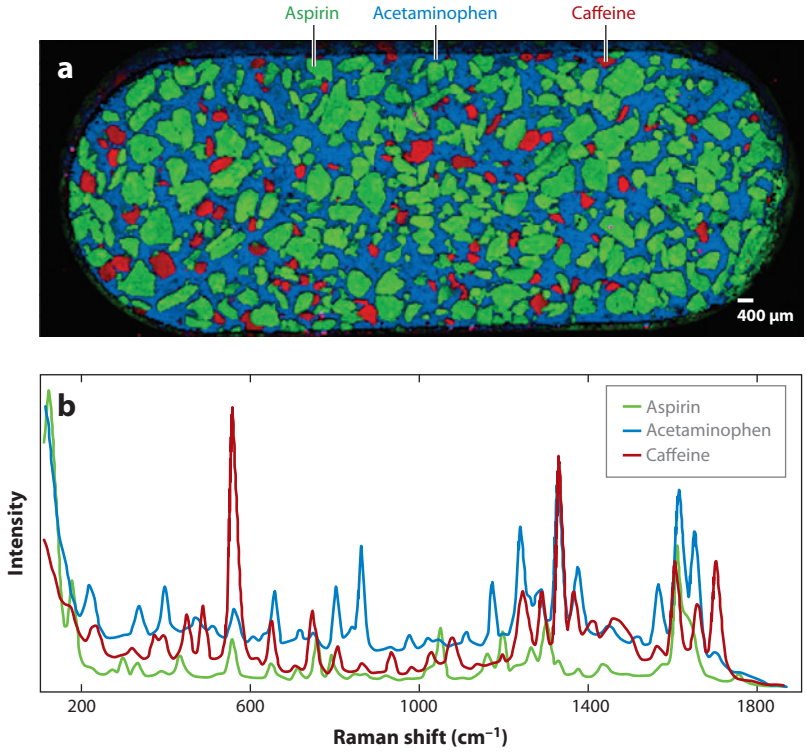

Figure 8

(*a*) False-colored Raman image of a pharmaceutical tablet from direct classical least squares score images. (*b*) Pure-ingredient Raman spectra of aspirin (*green*), acetaminophen (*blue*), and caffeine (*red*). Reproduced from Reference 77 with permission.

around a core with a polymer coating or compress the drug between an inert core and several polymer layers. In both cases, it is crucial that the coating be consistently applied. Scanning and mapping Raman microscopy, in conjunction with chemometric techniques, has been utilized to determine the chemical distribution of rapamycin/PLGA [poly(lactic-*co*-glycolic acid)] coatings on stents (82) and of isoptin SR-E (Meltrex®) in an extrusion manufacturing process (83).

Identification of polymorphs, unique crystal packing lattice forms of molecules, is another important aspect of pharmaceutical analysis. Single-crystal forms of APIs are greatly desired in the pharmaceutical industry, and Raman imaging is routinely used for their identification or quantification. In a recent study, Henson & Zhang (84) detected a polymorphic impurity in a tablet at a concentration of 0.05% by weight. In another study, spatially directed agglomeration clustering, in combination with Raman mapping, was applied to the analysis of two chloramphenicol palmitate polymorph forms across the surface of a tablet. This research was extended to drug tablets of varying weight percents, and a supervised learning method was utilized for validation purposes (85).

The ability to control drug-particle size and surface area leads to better drug solubility, improved drug bioavailability, and greater drug uptake rate, thereby allowing for well-controlled drug dosage and administration. Given the growing market of OINDPs, monitoring drug-particle size is of principal interest in the pharmaceutical field. Ingredient-specific particle sizing (ISPS™) is the analysis of the morphology of a unique chemical within a sample formulation performed with

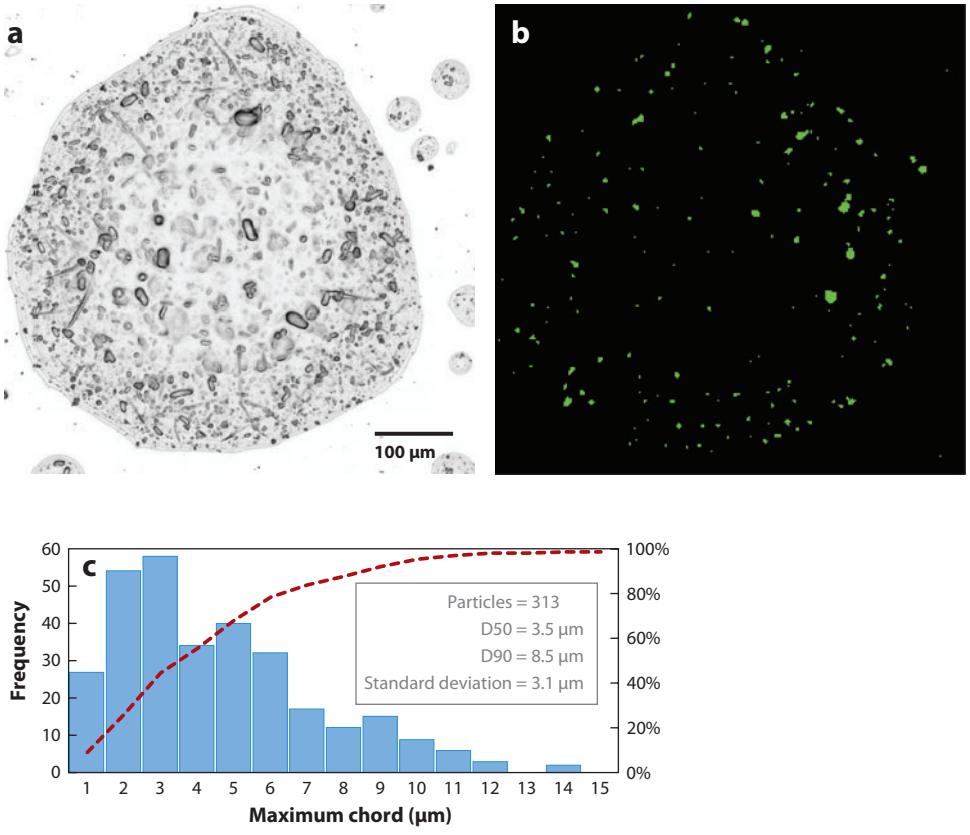

Figure 9

(*a*) Bright-field reflectance optical image of a Rhinocort Aqua droplet. (*b*) A corresponding Raman image of the budesonide particles. (*c*) The maximum chord particle-size distribution of budesonide in Rhinocort Aqua. Reproduced from Reference 87 with permission.

wide-field Raman imaging. In 2007, Doub et al. (86) described the ISPS methodology as applied to a nasal spray suspension formulation containing beclomethasone dipropionate (BDP) as the API. The authors observed good specificity for the BDP particles, which were clearly distinguishable from excipient particles (86). Priore et al. (87) later demonstrated an automated ISPS technique. **Figure 9** illustrates an example data set based on the automated ISPS method applied to a nasal spray formulation.

API-specific Raman imaging has been extended to dry powder inhalation systems (88). Lactose carrier particles were recently studied with regard to their ability to attach to drug particles for delivery. Wide-field Raman imaging permitted reasonably rapid analysis and clearly identified the API attached to the lactose carrier molecules (89).

3.2. Biomedicine

Whether used for the study of drug transport through live cells or for the assessment of early detection of brain cancer, Raman imaging in biomedicine has become a prime object of investigation in both the research and clinical settings (90). Improved spectrometers, microscopes,

and detection devices have facilitated the study of cells and cellular components. In one of the earliest reports, Raman images were used to assess lipid and protein distribution in chicken tissue (91). Bone tissue research has benefited from the emergence of Raman imaging due to the high Raman scattering properties of the minerals in bone. Line-scanned Raman images illustrate hydroxyapatite distribution in implants (92), bone maturity (93), and fatigue (94).

Cellular proteins, DNA, RNA, lipids, nuclei, and various other organelles in freeze-dried, living, and apoptotic cells have been observed in Raman images (95–98). Wide-field Raman imaging has been used to demonstrate mammalian cell viability (99) and three-dimensional profiling of a single cell (100). Advances in optical trapping technology have enabled the collection of Raman mapped images of living cells in suspension (101). Identification and quantification of waterborne pathogens have also been assessed with wide-field Raman imaging (102–105). Metabolism in bacterial cells (51) and growth of fungal cells have been observed with the use of SERS imaging (49).

Biomedical applications have been widely investigated with coherent Raman scattering approaches (33). Imaging of viruses, cells, tissues, and live animals has benefited from the high speed and sensitivity of CARS and SRS. These methods are highly sensitive to CH_2-rich molecular structures (29, 106–111) and thus have been extensively applied to lipid-based systems in cells (107, 112–114), tissues (115, 116), and whole organisms (117, 118).

The potential for Raman imaging to be used as a clinical tool has been noted by numerous researchers and clinicians (119–123) and demonstrated by several groups. In one study, Raman mapped images illustrated differences between normal brain tissue and intercranial tumors,

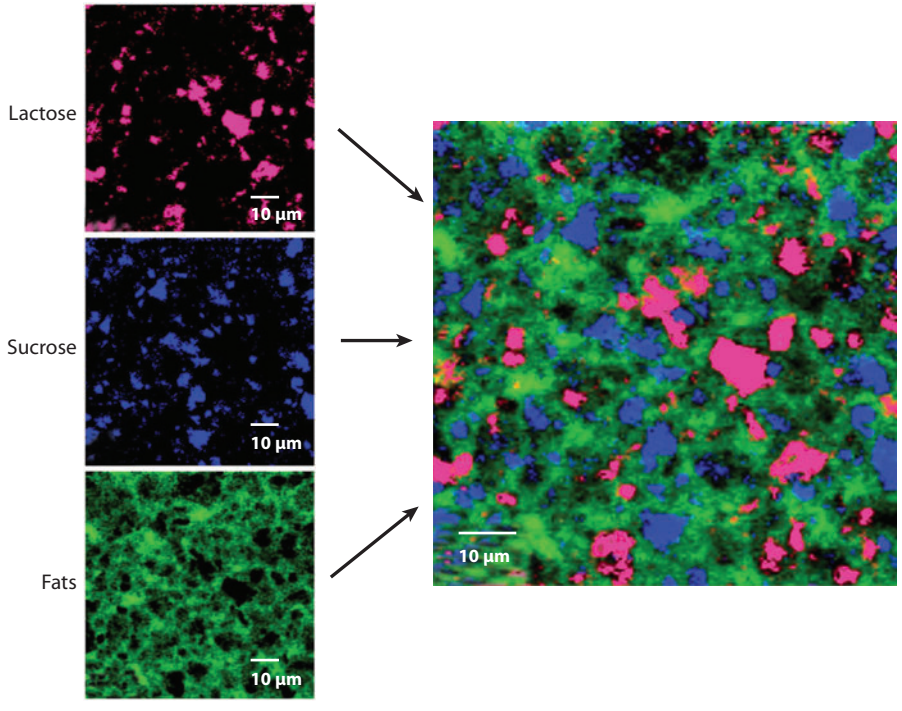

Figure 10

Raman mapping of a white chocolate sample measured at 532 nm, constituent maps, and the combined Raman map that shows the lactose and sucrose particles within a matrix of fats. Reproduced from Reference 133 with permission.

gliomas, and meningiomas (124). In another, Chao et al. (125) used nanometer-sized diamond particles as SERS probes to biolabel human lung epithelial cells. The cells were observable with SERS imaging. In research reported by the Gambhir group (48, 54), SERS nanoparticles were injected into a live mouse and observed in the mouse's liver through the collection of SERS mapped images through the skin.

The contribution of CARS and SRS to clinical applications has been demonstrated in numerous studies, despite their limiting, complex experimental requirements. The high contrast provided by these techniques is similar to that which can be obtained with conventional histochemical staining (126), and monitoring of small molecules such as drugs and metabolites inside tissue has been reported (113). Fiber-delivered CARS imaging technology has attracted attention because of its application to endoscopy (127–131).

3.3. Food

Due to the complex, heterogeneous nature of foodstuffs, routine characterization is a challenging process requiring multiple sample-preparation steps in addition to lengthy wet chemical analyses. The use of Raman imaging in the food industry has extended to various inspection and research and development applications, principally in bulk (20).

The requirement for minimal sample preparation has been exploited to measure food content and uniformity with Raman imaging. Microscopic Raman imaging has been applied to carrot

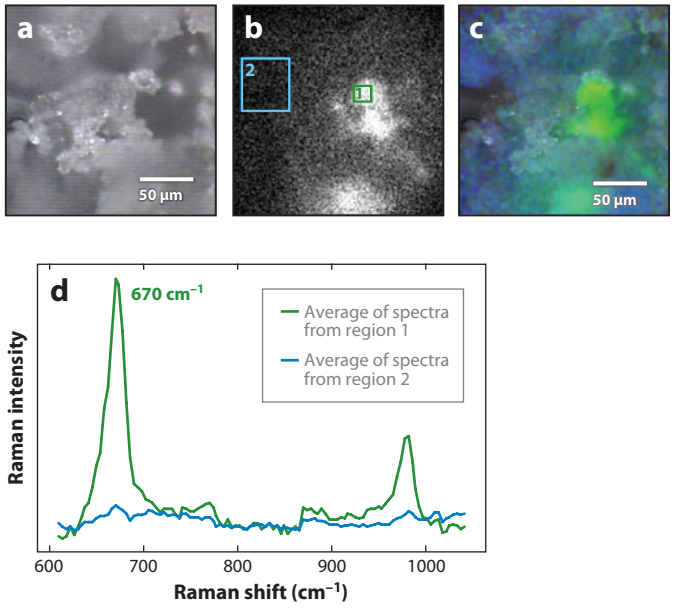

Figure 11

(*a*) Bright-field reflection image. (*b*) Corresponding Raman chemical image at 670 cm^{-1}. (*c*) Fusion of false-colored Raman chemical image with the corresponding bright-field reflection image. (*d*) Image spectrometer–derived spectra of selected regions of a sample containing a 6%-by-weight mixture of melamine in wheat flour. The laser power at the sample, with a 10× objective, was 460 mW. The melamine in the wheat flour mixture was prepared and supplied to the ChemImage Corporation by the U.S. Department of Agriculture, Agricultural Research Service (136). Reproduced from Reference 136 with permission.

(*Daucus carota* L.) roots in order to understand the distribution of polyacetylene, carotenoid, and polysaccharide components (132). Other food ingredients, such as sucrose, lactose, and fat constituents of white and milk chocolate, have also recently been studied with microscopic Raman imaging. Sucrose and lactose formed discrete particles within a fat matrix, and the spatial information was used to understand the morphology of these particles (**Figure 10**) (133). Recently, emulsion interfaces were studied in mayonnaise, cheese, and soy-based beverages (134).

Monitoring and inspection of food products have also been carried out with the Raman imaging methodology. A recent Raman-based approach for monitoring the maturity of tomatoes was performed through the observation of lycopene content. A point-mapping Raman imaging system interrogated tomato samples internally at varying levels of ripening and compared the acquired spectra with a pure spectrum of lycopene (135).

Wide-field Raman imaging can be utilized to observe pathogens in food (20). Identification of melamine in a wheat flour matrix by Raman imaging illustrates the potential of this methodology as a screening tool for food contamination. The Raman image in **Figure 11** was obtained on a ChemImage Raman imaging system equipped with 785-nm laser excitation. Priore et al. (137) continued this study with the fusion of Raman imaging with NIR imaging to increase the sensitivity and selectivity of a food-screening method.

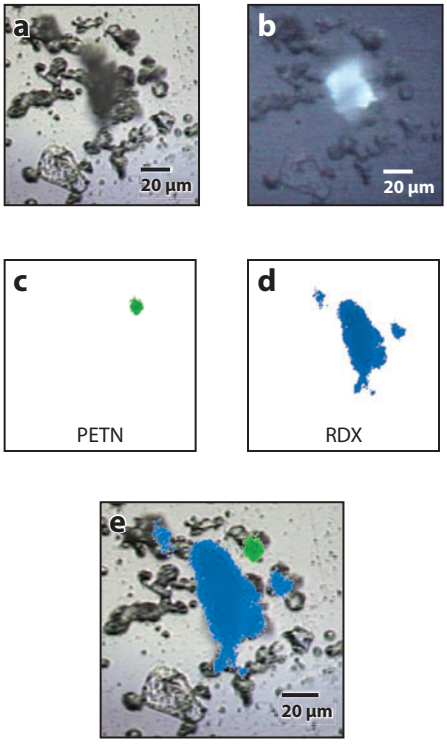

Figure 12

Images of a fingerprint contaminated with PETN (pentaerythritol tetranitrate) and RDX (research department explosive). (*a*) Bright-field image. (*b*) Fluorescence chemical image. (*c*) Raman chemical image (RCI) corresponding to PETN. (*d*) RCI corresponding to RDX. (*e*) Overlay of the RCIs on the bright-field image. Reproduced from Reference 139 with permission.

3.4. Threat Detection

The development of sensor systems for detecting the presence of chemical and biological threat materials and explosives has increased during the past decade. The detection of bulk and residue explosives and their precursors, especially in the presence of complex backgrounds, has been a significant focus of research in this field. The detection of Raman images of bulk materials such as ammonium nitrate, 2,4,6-trinitrotoluene, and nitromethane, in addition to devices such as improvised explosive devices (IEDs), has been demonstrated at standoff distances of 10 m (57).

High sensitivity is needed for the detection of trace explosives, which can be acquired by touching devices such as IEDs. Gresham et al. (138) determined that a typical mass of a first-order fingerprint obtained by touching explosives is on the order of a few micrograms. Raman imaging of trace explosive residues and precursors from fingerprints has been conducted at a standoff distance of 10 m (56). Tripathi et al. (139) used Raman hyperspectral imaging to detect contaminated fingerprints on strongly scattering plastic and painted metal backgrounds. These authors used partial least squares subtraction to minimize interfering substrate materials in the images, which resulted in increased image contrast for locating traces of explosives (**Figure 12**).

4. CONCLUDING REMARKS

Raman imaging is trending toward rapid, cost effective, and high spatial and spectral resolution imaging across the biomedical, pharmaceutical, and threat-detection industries. The biomedical industry is at the center of current Raman imaging research, where CARS, SRS, and SORS are redefining Raman as a potential routine analytical test. Commercialization of these point-mapping technologies will enable researchers to observe chemical contrast at the cellular level. Compressive sensing will allow both Raman mapping and wide-field imaging instrumentation to quickly measure the magnitude of an analytical signal in complex matrices across the pharmaceutical and threat-detection industries. Rapid ingredient-specific particle sizing based on Raman imaging will affect the pharmaceuticals that we consume as well as confirm or reject potential threat agents in the battlefield.

DISCLOSURE STATEMENT

The authors are not aware of any affiliations, memberships, funding, or financial holdings that might be perceived as affecting the objectivity of this review.

LITERATURE CITED

1. Delhaye M, Dhamelincourt P. 1975. Raman microprobe and microscope with laser excitation. *J. Raman Spectrosc.* 3:33–43
2. Boogh L, Meier R, Kausch H. 1992. A Raman microscopy study of stress transfer in high performance epoxy composites reinforced with polyethylene fibers. *J. Polym. Sci. Part B Polym. Phys.* 30:325–33
3. Clark D, Henson M, LaPlant F, Šašić S, Zhang L. 2007. Pharmaceutical applications of chemical mapping and imaging. In *Applications of Vibrational Spectroscopy in Pharmaceutical Research and Development*, ed. DE Pivonka, JM Chalmers, PR Griffiths, 3:309–35. London: Wiley
4. Everall N. 2004. Depth profiling with confocal Raman microscopy. Part I. *Spectroscopy* 19:22–28
5. Everall N. 2004. Depth profiling with confocal Raman microscopy. Part II. *Spectroscopy* 19:16–27
6. Bowden M. Gardiner D, Rice G, Gerrand D. 1990. Line-scanned micro Raman spectroscopy using a cooled CCD imaging detector. *J. Raman Spectrosc.* 21:37–41
7. Jestel N, Shaver J, Morris M. 1998. Hyperspectral Raman line imaging of an aluminosilicate glass. *Appl. Spectrosc.* 52:64–69

8. Markwort L, Kip B. 1996. Micro-Raman imaging of heterogeneous polymer systems: general applications and limitations. *J. Appl. Polym. Sci.* 61:231–54
9. Morris H, Hoyt C, Miller P, Treado P. 1996. Liquid crystal tunable filter Raman chemical imaging. *Appl. Spectrosc.* 50:805–11
10. Puppels G, Grond M, Greve J. 1993. Direct imaging Raman microscope based on tunable wavelength excitation and narrow-band emission detection. *Appl. Spectrosc.* 47:1256–67
11. Schaeberle M, Karakatsanis C, Lau C, Treado P. 1995. Raman chemical imaging: noninvasive visualization of polymer blend architecture. *Anal. Chem.* 67:4316–21
12. Treado P, Levin I, Lewis E. 1992. High-fidelity Raman imaging spectrometry: a rapid method using an acousto-optic tunable filter. *Appl. Spectrosc.* 46:1211–16
13. Goldstein S, Kidder L, Herne T, Levin I, Lewis E. 1996. The design and implementation of a high-fidelity Raman imaging microscope. *J. Microsc.* 184:35–45
14. Turner J II, Treado P. 1997. LCTF Raman chemical imaging in the near infrared. *Proc. SPIE* 3061:280–83
15. Nelson M, McLestar M, Aust J, Myrick M. 1996. *Distributed sensing of fiber-optic arrays*. Presented at Pittsburgh Conf. Expo. Anal. Chem. Appl. Spectrosc., Chicago
16. Nelson M, Myrick M. 1999. Single-frame chemical imaging: dimension reduction fiber-optic array improvements and application to laser-induced breakdown spectroscopy. *Appl. Spectrosc.* 53:751–59
17. Nelson M, Bell W, McLester M, Myrick M. 1998. Single-shot multiwavelength imaging of laser plumes. *Appl. Spectrosc.* 52:179–86
18. Nelson M, Myrick M. 1999. Fabrication and evaluation of a dimension-reduction fiber optic system for chemical imaging applications. *Rev. Sci. Instrum.* 70:2836–44
19. Ma J, Ben-Amotz D. 1997. Rapid micro-Raman imaging using fiber-bundle image compression. *Appl. Spectrosc.* 51:1845–48
20. Treado PJ, Priore RJ, Nelson MP. 2010. Raman spectroscopic imaging. In *Applications of Vibrational Spectroscopy in Food Science*, ed. ECY Li-Chan, PR Griffiths, JM Chalmers, pp. 156–94. Hoboken: Wiley
21. Treado P, Nelson M. 2001. Raman imaging. In *Handbook of Raman Spectroscopy from the Research Laboratory to the Process Line*, Vol. 5: *Practical Spectroscopy*, ed. I Lewis, H Edwards, pp. 191–250. New York: Marcel Dekker
22. Morris H, Hoyt C, Treado P. 1994. Imaging spectrometers for fluorescence and Raman microscopy: acousto-optic and liquid crystal tunable filters. *Appl. Spectrosc.* 48:857–66
23. Wang X, Voigt T, Bos P, Nelson M, Treado P. 2006. Evaluation of a high-throughput liquid crystal tunable filter for Raman chemical imaging of threat materials. *Proc. SPIE* 6378:637808
24. Evans J. 1958. Solc birefringent filter. *J. Opt. Soc. Am.* 48:142–43
25. Lyot B. 1944. The birefringent filter and its application in solar physics. *Ann. Astrophys.* 7:31–36
26. Treado PJ, Nelson MP, Schweitzer R, Gardner C, Wentworth R. 2008. Standoff Raman hyperspectral imaging detection of explosives. In *Laser Applications to Chemical, Security and Environmental Analysis*, pap. LThB1. St. Petersburg, Fla.: Opt. Soc. Am.
27. Maker PD, Terhune RW. 1965. Study of optical effects due to an induced polarization third order in the electric field strength. *Phys. Rev. A* 137:801–18
28. Zumbusch A, Holtom GR, Xie XS. 1999. Three-dimensional vibrational imaging by coherent anti-Stokes Raman scattering. *Phys. Rev. Lett.* 82:4142–45
29. Evans CL, Xie XS. 2008. Coherent anti-Stokes Raman scattering microscopy: chemical imaging for biology and medicine. *Annu. Rev. Anal. Chem.* 1:883–909
30. Wang H, Fu Y, Zickmund P, Shi R, Cheng J-X. 2005. Coherent anti-Stokes Raman scattering imaging of axonal myelin in live spinal tissues. *Biophys. J.* 89:1–11
31. Cheng JX, Xie XS. 2004. Coherent anti-Stokes Raman scattering microscopy: instrumentation, theory and applications. *J. Phys. Chem.* 108:827–40
32. Evans CL, Potma EO, Puoris'haag M, Cote D, Lin CP, Xie XS. 2005. Chemical imaging of tissue in vivo with video-rate coherent anti-Stokes Raman scattering microscopy. *Proc. Natl. Acad. Sci. USA* 102:16807–12
33. Wang Z, Gao L, Juo P, Yang Y, Hammoundi AA, et al. 2011. Coherent anti-Stokes Raman scattering microscopy imaging with suppression of four-wave mixing in optical fibers. *Opt. Express* 19:7960–70

34. Kim S-H, Lee E-S, Lee JY, Lee ES, Lee B-S, et al. 2010. Multiplex coherent anti-Stokes Raman spectroscopy images intact atheromatous lesions and concomitantly identifies distinct chemical profiles of atherosclerotic lipids. *Circ. Res.* 106:1–10
35. Min W, Freudiger CW, Lu S, Xie XS. 2011. Coherent nonlinear optical imaging: beyond fluorescence microscopy. *Annu. Rev. Phys. Chem.* 62:507–30
36. Potma EO. 2010. Tissue imaging with coherent anti-Stokes Raman scattering microscopy. In *Vibrational Spectroscopic Imaging for Biomedical Applications*, ed. G Srinivasan, 11:319–47. New York: McGraw Hill
37. Owyoung A. 1978. Coherent Raman gain spectroscopy using CW laser sources. *IEEE J. Quantum Electron.* 14:192–203
38. Levine BF, Shank CV, Heritage JP. 1979. Surface vibrational spectroscopy using stimulated Raman scattering. *IEEE J. Quantum Electron.* 15:1418–32
39. Levenson MD, Moerner WE, Horne DE. 1983, FM spectroscopy detection of stimulated Raman gain. *Opt. Lett.* 8:108–10
40. Levenson MD, Kano SS. 1988. *Introduction to Nonlinear Laser Spectroscopy.* San Diego: Academic. 299 pp.
41. Boyd RW. 2003. *Nonlinear Optics.* London: Academic. 613 pp.
42. Freudiger CW, Min W, Holtom GR, Xu B, Dantus M, Xie XS. 2011. Highly specific label-free molecular imaging with spectrally tailored excitation-stimulated Raman scattering (STE-SRS) microscopy. *Nat. Photonics* 5:103–9
43. McGlashen ML, Guhathakurta U, Davis KL, Morris MD. 1991. SERS microscopy: laser illumination effects. *Appl. Spectrosc.* 45:543–45
44. Evans SD, Freeman TL, Flynn TM, Batchelder DN, Ulman A. 1994. Raman spectroscopy of self-assembled mono- and multilayer films of alkanethiolate on gold. *Thin Solid Films* 244:778–83
45. Kenipp K, Moskovits M, Kneipp H, eds. 2006. *Surface-Enhanced Raman Scattering: Physics and Applications.* Berlin/ Heidelberg: Springer. 464 pp.
46. Kneipp J, Kneipp H, Kneipp K. 2008. SERS—a single-molecule and nanoscale tool for bioanalysis. *Chem. Soc. Rev.* 37:1052–60
47. Schwartzberg AM, Zhang JZ. 2008. Novel optical properties and emerging applications of metal nanostructures. *J. Phys. Chem. C* 112:10323–37
48. Keren S, Zavaleta C, Cheng Z, de la Zerda A, Gheysens O, Gambhir S. 2008. Noninvasive molecular imaging of small living subjects using Raman spectroscopy. *Proc. Natl. Acad. Sci. USA* 105:5844–849
49. Gough KM, Kaminskyj SGW. 2010. sFTIR, Raman, and SERS imaging of fungal cells. In *Vibrational Spectroscopic Imaging for Biomedical Applications*, ed. G. Srinivasan, pp. 125–56. New York: McGraw Hill
50. Fujita K, Ishitobi S, Hamada K, Smith NI, Taguchi A, et al. 2009. Time-resolved observation of surface-enhanced Raman scattering from gold nanoparticules during transport through a living cell. *J. Biomed. Opt.* 14:024038
51. Ravindranath SP, Henne KL, Thompson DK, Irudayaraj J. 2011. Surface-enhanced Raman imaging of intracellular bioreduction of chromate in *Shewanella oneidensis*. *PLoS ONE* 6:e16634
52. Lee M, Lee S, Lee J, Lim H, Seong GH, et al. 2011. Highly reproducible immunoassay of cancer markers on a gold-patterned microarray chip using surface-enhanced Raman scattering imaging. *Biosens. Bioelectron.* 26:2135–41
53. Lee S, Chon H, Lee M, Choo J, Shin SY, et al. 2009. Surface-enhanced Raman scattering imaging of HER2 cancer markers overexpressed in single MCF7 cells using antibody conjugated hollow gold nanospheres. *Biosens. Bioelectron.* 24:2260–63
54. Zavaleta CL, Smith BR, Walton I, Doering W, Davis G, et al. 2009. Multiplexed imaging of surface enhanced Raman scattering nanotags in living mice using noninvasive Raman spectroscopy. *Proc. Natl. Acad. Sci. USA* 106:13511–16
55. Sharma SK, Misra AK, Sharma B. 2005. Portable remote Raman system for monitoring hydrocarbon, gas hydrates and explosives in the environment. *Spectrochim. Acta A* 61:2402–12
56. Nordberg M, Adkeson M, Ostmark H, Carlsson TE. 2011. Stand-off detection of explosive particles by imaging Raman spectroscopy. *Proc. SPIE* 8017:80171B
57. Pettersson A, Wallin S, Ostmark H, Ehlerding A, Johansson I, et al. 2010. Explosives standoff detection using Raman spectroscopy: from bulk towards trace detection. *Proc. SPIE* 7664:76641K

58. Bremer MT, Lozovoy VV, Dantus M. 2011. Standoff chemical imaging of trace quantities using single-beam CARS. *Proc. CLEO 2011*, pap. CFF5
59. Matousek P, Clark IP, Draper ERC, Morris MD, Goodship AE, et al. 2005. Subsurface probing in diffusely scattering media using spatially offset Raman spectroscopy. *Appl. Spectrosc.* 59:393–400
60. Matousek P, Clark IP, Draper ERC, Morris MD, Goodship AE, et al. 2005. Numerical simulations of subsurface probing in diffusely scattering media using spatially offset Raman spectroscopy. *Appl. Spectrosc.* 59:1485–92
61. Macleod NA, Matousek P. 2008. Deep noninvasive Raman spectroscopy of turbid media. *Appl. Spectrosc.* 62:291–304A
62. Matousek P, Draper ERC, Goodship AE, Clark IP, Ronayne KL, Parker AW. 2006. Noninvasive Raman spectroscopy of human tissue in vivo. *Appl. Spectrosc.* 60:758–63
63. Matousek P. 2006. Inverse spatially offset Raman spectroscopy for deep noninvasive probing of turbid media. *Appl. Spectrosc.* 60:1341–47
64. Eliasson C, Claybourn M, Matousek P. 2007. Deep subsurface Raman spectroscopy of turbid media by a defocused collection system. *Appl. Spectrosc.* 61:1123–27
65. Stone N, Faulds K, Graham D, Matousek P. 2010. Prospects of deep Raman spectroscopy for noninvasive detection of conjugated surface enhanced resonance Raman scattering nanoparticles buried within 25 mm of mammalian tissue. *Anal. Chem.* 82:3969–73
66. Stone N, Kerssens M, Lloyd GR, Faulds K, Graham D, Matousek P. 2011. Surface enhanced partially offset Raman spectrocopic (SESORS) imaging—the next dimension. *Chem. Sci.* 2:776–80
67. Schulmerich MV, Cole JH, Dooley KA, Morris, MD, Kreider JM, et al. 2008. Noninvasive Raman tomographic imaging of canine bone tissue. *J. Biomed. Opt. Lett.* 13:020506
68. Baraniuk RG. 2007. Compressive sensing. *IEEE Signal Process. Mag.* 24:118–21
69. Candes EJ, Romber J, Tao T. 2006. Stable signal recovery from incomplete and inaccurate measurements. *Commun. Pure Appl. Math.* 59:1207–23
70. Nelson MP, Aust JF, Dobrowolski JA, Verly PG, Myrick ML. 1998. Multivariate optical computation for predictive spectroscopy. *Anal. Chem.* 70:73–82
71. Priore RJ, Haibach FG, Schiza MV, Greer AE, Perkins DL, Myrick ML. 2004. Miniature stereo spectral imaging system for multivariate optical computing. *Appl. Spectrosc.* 58:870–73
72. Myrick ML, Soyemi OO, Haibach FG, Zhang L, Greer AE, et al. 2002. Application of multivariate optical computing to near-infrared imaging. *Proc. SPIE* 4577:148–57
73. Quyen N, Da Silva E, Dao NQ, Jouan MD. 2006. New Raman spectrometer using a digital micromirror device and a photomultiplier tube detector for rapid on-line industrial analysis. Part I: Description of the prototype and preliminary results. *Appl. Spectrosc.* 62:273–78
74. Uzunbajakava N, de Peinder P, 't Hooft GW, van Gogh ATM. 2006. Low-cost spectroscopy with a variable multivariate optical element. *Anal. Chem.* 78:7302–8
75. Davis BM, Hemphill AJ, Maltas DC, Zipper MA, Wang P, Ben-Amotz D. 2011. Multivariate hyperspectral Raman imaging using compressive detection. *Anal. Chem.* 83:5086–92
76. Gendrin C, Roggo Y, Collet C. 2008. Pharmaceutical applications of vibrational chemical imaging and chemometrics: a review. *J. Pharm. Biomed. Anal.* 48:533–53
77. Nelson M, Treado P. 2010. Raman imaging instrumentation. In *Raman, Infrared, and Near-Infrared Chemical Imaging*, ed. S Šašić, Y Ozaki, 2:23–54. Hoboken: Wiley
78. Šašić S. 2007. An in-depth analysis of Raman and near-infrared chemical images of common pharmaceutical tablets. *Appl. Spectrosc.* 61:239–50
79. Šašić S. 2008. Chemical imaging of pharmaceutical granules by Raman global illumination and near-infrared mapping platforms. *Anal. Chim. Acta* 611:73–79
80. Widjaja E, Kim R, Seah H. 2008. Application of Raman microscopy and band-target entropy minimization to identify minor components in model pharmaceutical tablets. *J. Pharm. Biomed. Anal.* 46:274–81
81. Slipchenko MN, Chen H, Ely DR, Jung Y, Carvajal MT, Cheng J. 2010. Vibrational imaging of tablets by epi-detected stimulated Raman scattering microscopy. *Analyst* 135:2613–19
82. Belu A, Mahoney C, Wormuth K. 2008. Chemical imaging of drug eluting coatings: combining surface analysis and confocal Raman microscopy. *J. Control. Release* 126:111–21

83. Vajna B, Pataki H, Nagy Z, Farkas I, Marosi G. 2011. Characterization of melt extruded and conventional Isoptin formulations using Raman chemical imaging and chemometrics. *Int. J. Pharm.* 419:107–13
84. Henson M, Zhang L. 2006. Drug characterization in low dosage pharmaceutical tablets using Raman microscopic mapping. *Appl. Spectrosc.* 60:1247–55
85. Lin W, Jiang J, Yang H, Ozaki Y, Shen G, Yu R. 2006. Characterization of chloramphenicol palmitate drug polymorphs by Raman mapping with multivariate image segmentation using a spatial directed agglomeration clustering method. *Anal. Chem.* 78:6003–11
86. Doub W, Adams W, Spencer J, Buhse L, Nelson M, Treado P. 2007. Raman chemical imaging for ingredient-specific particle size characterization of aqueous suspension nasal spray formulations: a progress report. *Pharm. Res.* 24:934–45
87. Priore RJ, Olkhovyk O, Klueva O, Fuhrman M. 2009. Automation of ingredient-specific particle sizing employing Raman chemical imaging. *RDD Eur.* 2:275–78
88. Theophilus A, Moore A, Prime D, Rossomanno S, Whitcher B, Chrystn H. 2006. Codeposition of salmeterol and fluticasone propionate by a combination inhaler. *Int. J. Pharm.* 313:14–22
89. Šašić S, Harding L. 2010. Global illumination Raman chemical imaging of a combination dry powder inhaler formulation. *Respir. Drug Deliv.* 3:729–32
90. Stewart S, Panza J, Drauch A. 2010. Widefield Raman imaging of cells and tissues. In *Vibrational Spectroscopic Imaging for Biomedical Applications*, ed. G Srinivasan, 6:157–91. New York: McGraw Hill
91. Kline N, Treado P. 1997. Raman chemical imaging of breast tissue. *J. Raman Spectrosc.* 28:119–24
92. Otto C, de Grauw J, Duindam J. 1997. Applications of micro-Raman imaging in biomedical research. *J. Raman Spectrosc.* 28:143–50
93. Timlin J, Carden A, Morris M, Bonadio J, Hoeffler C II, et al. 1999. Spatial distribution of phosphate species in mature and newly generated mammalian bone by hyperspectral Raman imaging. *J. Biomed. Opt.* 4:28–34
94. Timlin J, Carden A, Morris M, Rajachar R, Kohn D. 2000. Raman spectroscopic imaging markers for fatigue-related microdamage in bovine bone. *Anal. Chem.* 72:2229–36
95. Uzunbajakava N, Leferink A, Kraan Y, Volokhina E, Vrensen G, et al. 2003. Nonresonant confocal Raman imaging of DNA and protein distribution in apoptotic cells. *Biophys. J.* 84:3968–81
96. Krafft C, Knetschke T, Siegner A, Funk RHW, Salzer R. 2003. Mapping of single cells by near infrared Raman microspectroscopy. *Vib. Spectrosc.* 32:75–83
97. Uzunbajakava N, Lenferink A, Kraan Y, Willekens B, Vrensen G, et al. 2003. Nonresonant Raman imaging of protein distribution in single human cells. *Biopolymers* 72:1–9
98. Matthaus C, Chemenko T, Newmark J, Warner C, Diem M. 2007. Label-free detection of mitochondrial distribution in cells by nonresonant Raman microspectroscopy. *Biophys. J.* 93:668–73
99. Panza J, Maier J. 2007. Raman spectroscopy and Raman chemical imaging of apoptotic cells. *Proc. SPIE* 6441:644108
100. Maier JS, Treado PJ. 2004. Raman molecular chemical imaging: 3D Raman using deconvolution. *Proc. SPIE* 5588:98–105
101. Creely C, Volpe B, Singh G, Soler M, Petrov D. 2005. Raman imaging of floating cells. *Opt. Express* 13:6105–10
102. Stewart S, McClelland L, Maier J. 2005. A fast method for detecting *Cryptosporidium parvum* oocysts in real world samples. *Proc. SPIE* 5692:341–50
103. Escoriza MF, Vanbriesen JM, Stewart S, Maier J, Treado PJ. 2006. Raman spectroscopy and chemical imaging for quantification of filtered waterborne bacteria. *J. Microbiol. Methods* 66:63–72
104. Kalasinsky K, Hadfield T, Shea A, Kalasinsky V, Nelson M, et al. 2007. Raman chemical imaging spectroscopy reagentless detection and identification of pathogens: signature development and evaluation. *Anal. Chem.* 79:2658–73
105. Tripathi A, Jabbour R, Treado P, Neiss J, Nelson M, et al. 2008. Waterborne pathogen detection using Raman spectroscopy. *Appl. Spectrosc.* 62:1–9
106. Cheng JX. 2007. Coherent anti-Stokes Raman scattering microscopy. *Appl. Spectrosc.* 61:197–208
107. Nan X, Cheng JX, Xie XS. 2003. Vibrational imaging of lipid droplets in live fibroblast cells with coherent anti-Stokes Raman scattering microscopy. *J. Lipid Res.* 44:2202–8

108. Muller M, Zumbusch A. 2007. Coherent anti-Stokes Raman scattering microscopy. *ChemPhysChem* 8:2156–70
109. Evans CL, Xu X, Kesari S, Xie XS, Wong STC, Young GS. 2007. Chemically selective imaging of brain structures with CARS microscopy. *Opt. Express* 15:12076–87
110. Cheng JX, Volkmer A, Book LD, Xie XS. 2002. Multiplex coherent anti-Stokes Raman scattering microspectroscopy and study of lipid vesicles. *J. Phys. Chem.* 106:8493–98
111. Muller M, Schins JM. 2002. Imaging of thermodynamic state of lipid membranes with multiplex CARS microscopy. *J. Phys. Chem. B* 106:3715–23
112. Nan X, Potma EO, Xie XS. 2006. Nonperturbative chemical imaging of organelle transport in living cells with coherent anti-Stokes Raman scattering microscopy. *Biophys. J.* 91:728–35
113. Freudiger CW, Min W, Saar BG, Lu S, Holtom GR, et al. 2008. Label-free biomedical imaging with high sensitivity by stimulated Raman scattering microscopy. *Science* 322:1857–61
114. Nandakumar P, Kovalev A, Volkmer A. 2009. Vibrational imaging based on stimulated Raman scattering microscopy. *New J. Phys.* 11:033026
115. Wang HW, Fu Y, Huff TB, Le TT, Wang H, Cheng JX. 2009. Chasing lipids in health and diseases by coherent anti-Stokes Raman scattering microscopy. *Vib. Spectrosc.* 50:160–67
116. Begin X, Belanger E, Laffray S, Cote VR. 2009. In vivo optical monitoring of tissue pathologies and diseases with vibrational contrast. *J. Biophotonics* 2:632–42
117. Enejder A, Brackmann C, Svedberg F. 2010. Coherent anti-Stokes Raman scattering microscopy of cellular lipid storage. *IEEE J. Sel. Top. Quantum Electron.* 16:506–15
118. Le TT, Duren HM, Slipchenko MN, Hu CD, Cheng JX. 2010. Label-free quantitataive analysis of lipid metabolism in living *Caenorhabditis elegans*. *J. Lipid Res.* 51:672–77
119. Chan JW, Taylor DS, Zwerdling T, Lane SM, Ihara K, Huser T. 2006. Micro-Raman spectroscopy detects individual neoplastic and normal hematopoietic cells. *Biophys. J.* 90:648–56
120. Krishna CM. 2006. Combined Fourier transform infrared and Raman spectroscopic approach for identification of multidrug resistance phenotype in cancer cell lines. *Biopolymers* 82:462–70
121. Kudelski A. 2008. Analytical applications of Raman spectroscopy. *Talanta* 76:1–8
122. Ramser K, Wenseleers W, Dewilde S, Van Doorslaer S, Moens L, Hanstorp D. 2007. A combined microresonance Raman and absorption set-up enabling in vivo studies under varying physiological conditions: the nerve globin in the nerve cord of aphrodite aculeate. *J. Biochem. Biophys. Methods* 70:627–33
123. Krishna CM, Sockalingum GD, Kegelaer G, Rubin S, Kartha VB, Manfait M. 2005. Micro-Raman spectroscopy of mixed cancer cell populations. *Vib. Spectrosc.* 38:95–100
124. Krafft C, Sobottka S, Schrackert G, Salzer R. 2005. Near infrared Raman spectroscopic mapping of native brain tissue and intracranial tumors. *Analyst* 130:1070–77
125. Chao J-I, Perevedentseva E, Chung P-H, Liu K-K, Cheng C-Y, et al. 2007. Nanometer-sized diamond particle as a probe for biolabeling. *Biophys. J.* 93:2199–208
126. Potma E, Cheng J-X, Xie XS. 2011. Coherent Raman imaging techniques and biomedical applications. *J. Biomed. Opt.* 16:021101
127. Wang H, Huff TB, Cheng J-X. 2006. Coherent anti-Stokes Raman scattering imaging with a laser source delivered by a photonic crystal fiber. *Opt. Lett.* 31:1417–19
128. Downes A, Mouras R, Elfick A. 2009. A versatile CARS microscope for biological imaging. *J. Raman Spectrosc.* 40:757–62
129. Balu M, Liu G, Chen Z, Tromberg BJ, Potma EO. 2010. Fiber delivered probe for efficient CARS imaging of tissues. *Opt. Express* 18:2380–88
130. Wang Z, Yang Y, Luo P, Gao L, Wong KK, Wong STC. 2010. Delivery of picosecond lasers in multimode fibers for coherent anti-Stokes Raman scattering imaging. *Opt. Express* 18:13017–28
131. Legare F, Evans CL, Ganikhanov F, Xie XS. 2006. Towards CARS endoscopy. *Opt. Express* 14:4427–32
132. Baranska M, Schultz H, Baranski R, Nothnagel T, Christensen LP. 2005. In situ simultaneous analysis of polyacetylenes, carotenoids and polysaccharides in carrot roots. *J. Agric. Food Chem.* 53:6565–71
133. Larmour IA, Faulds K, Graham D. 2010. Rapid Raman mapping for chocolate analysis. *Anal. Methods* 2:1230–32
134. Roeffaers MB, Zhang X, Freudiger CW, Saar BG, van Ruijven M, et al. 2011. Label-free imaging of biomolecules in food products using stimulated Raman microscopy. *J. Biomed. Opt.* 16:066016

135. Qin J, Chao K, Kim MS. 2011. Evaluating carotenoid changes in tomatoes during postharvest ripening using Raman chemical imaging. *Proc. SPIE* 8027:802703
136. Liu Y, Chao K, Kim M, Tuschel D, Olkhovyk O, Priore R. 2009. Potential of Raman spectroscopy and imaging methods for rapid and routine screening of the presence of melamine in animal feed and foods. *Appl. Spectrosc.* 63:477–80
137. Priore RJ, Olkhovyk O, Drauch A, Treado P, Kim M, Chao M. 2009. Recent advances in chemical imaging technology for the detection of contaminants for food safety and security. *Proc. SPIE* 7315:731507
138. Gresham GL, Davies JP, Goodrich LD, Blackwood LG, Liu BY, et al. 1994. Development of particle standards for testing detection systems: mass of RDX and particle size distribution of composition 4 residues. *Proc. SPIE* 2276:34–44
139. Tripathi A, Emmons ED, Wilcox PG, Guicheteau JA, Emge DK, et al. 2011. Semi-automated detection of trace explosives in fingerprints on strongly interfering surfaces with Raman chemical imaging. *Appl. Spectrosc.* 65:611–19

Annual Review of
Analytical Chemistry

Volume 5, 2012

Contents